Noninvasive glucose sensing by transcutaneous Raman spectroscopy

Wei-Chuan Shih
Kate L. Bechtel
Mihailo V. Rebec

Noninvasive glucose sensing by transcutaneous Raman spectroscopy

Wei-Chuan Shih,[a,b,c,*] **Kate L. Bechtel,**[c,†] **and Mihailo V. Rebec**[d]
[a]University of Houston, Department of Electrical and Computer Engineering, 4800 Calhoun Road, Houston, Texas 77204, United States
[b]University of Houston, Department of Biomedical Engineering, 4800 Calhoun Road, Houston, Texas 77204, United States
[c]Spectroscopy Laboratory, Massachusetts Institute of Technology, Cambridge, Massachusetts 02139, United States
[d]iSense CGM, 27700SW 95th Avenue, Wilsonville, Oregon 97070, United States

Abstract. We present the development of a transcutaneous Raman spectroscopy system and analysis algorithm for noninvasive glucose sensing. The instrument and algorithm were tested in a preclinical study in which a dog model was used. To achieve a robust glucose test system, the blood levels were clamped for periods of up to 45 min. Glucose clamping and rise/fall patterns have been achieved by injecting glucose and insulin into the ear veins of the dog. Venous blood samples were drawn every 5 min and a plasma glucose concentration was obtained and used to maintain the clamps, to build the calibration model, and to evaluate the performance of the system. We evaluated the utility of the simultaneously acquired Raman spectra to be used to determine the plasma glucose values during the 8-h experiment. We obtained prediction errors in the range of $\sim 1.5 - 2$ mM. These were in-line with a best-case theoretical estimate considering the limitations of the signal-to-noise ratio estimates. As expected, the transition regions of the clamp study produced larger predictive errors than the stable regions. This is related to the divergence of the interstitial fluid (ISF) and plasma glucose values during those periods. Two key contributors to error beside the ISF/plasma difference were photobleaching and detector drift. The study demonstrated the potential of Raman spectroscopy in noninvasive applications and provides areas where the technology can be improved in future studies. © *2015 Society of Photo-Optical Instrumentation Engineers (SPIE)* [DOI: 10.1117/1.JBO.20.5.051036]

1 Introduction

Applications of spectroscopy techniques to biological and biomedical problems have been rapidly advancing in recent years.[1–3] Based on inelastic scattering, Raman spectroscopy, as a type of vibrational spectroscopy, provides extremely rich molecular information about multiple chemical species present in a sample/specimen simultaneously.[4–13] The intensity of a Raman signal bears a linear relationship to the analyte concentrations, therefore, Raman spectroscopy can be used as a quantitative tool in concentration measurements as well.[1,4,5,14–17] An ultimate goal in this field is to develop Raman spectroscopy-based techniques for biomedical applications through instrumentation,[18–22] plasmonic substrates,[23–27] devices,[28,29] assays,[30,31] and techniques.[32,33]

Raman spectroscopic measurements, like other optical techniques, pose minimal danger from exposure to ionizing radiation due to the low-energy optical radiation exposure. One additional advantage of the NIR source used in Raman is that the tissue sampling region is much deeper than those provided by other optical approaches due to the reduced tissue scattering and reduced water and chromophore absorption at those wavelengths. As a result, NIR Raman spectroscopy satisfies two critical prerequisites for a truly noninvasive technique to transcutaneously monitor clinically important chemicals *in vivo*.[14,21,34–36] Nevertheless, noninvasive techniques of this kind will be valuable in a wide variety of clinical settings and laboratory tests.

We have employed multivariate calibration techniques such as partial least squares (PLS) and constrained regularization to noninvasive glucose sensing using Raman spectroscopy.[1,14,16,17] Glucose is a convenient analyte to study because its concentration can be conveniently altered and monitored in humans and other living animals such as dogs. The dog model provides several advantages such as a similar physiological glucose response as humans, no motion artifacts owing to the anesthesia that can be administered, and the flexibility to perform glucose clamping studies.

The dog study described in this paper was performed on a beagle anesthetized for ~ 8 h, during which its blood glucose concentration was clamped at several different levels. Raman spectra were continuously acquired from the ear and reference blood glucose measurements were taken using plasma glucose obtained from venous blood draws. Results from PLS analyses demonstrate that the calibration model can predict samples that were not included in the calibration set. The PLS analysis included a leave-one-level-out analysis, and thus represents a step in the direction of a completely prospective analysis.

2 Methods

2.1 Raman System

The Raman system for this study was modified from the previously published version for human volunteers.[14] The geometry of the light delivery path was modified to allow the excitation

*Address all correspondence to: Wei-Chuan Shih, E-mail: wshih@uh.edu

†Current address: Triple Ring Technologies, Newark, California, United States

laser to have normal incidence from beneath the dog ear through a hole in the paraboloidal mirror that subsequently collects and collimates the backscattered Raman signal. In other words, a mirror was placed underneath the paraboloidal mirror to redirect the originally in-plane optical path to be perpendicular to the optical plane. Figure 1 shows the equivalent optical path after folding the perpendicular path in-plane. The dog ear was placed in contact with a sapphire window embedded within an aluminum platform, with the backside of the window serving as a reference plane. The optimal distance between the reference plane and the paraboloidal mirror was determined by maximizing the intralipid Raman signal from a tissue phantom contained in a sample holder simulating the dog ear geometry, i.e., a 1.5 (radius) × 0.2 (thickness) cm cylindrical tissue phantom solution with optical properties and a thickness close to the dog ear. Figure 2 shows an aluminum sample stage where a dog subject can lie on its stomach with its ear positioned over the sapphire window aperture.

2.2 Experimental Protocol

The dog was maintained under an isoflourane inhaled anesthetic for the duration of the study. The blood glucose levels were clamped at eight levels for a period of 45 min at each level. These glucose levels were achieved and maintained by infusing 20% dextrose and insulin into ear veins. Blood samples were drawn every 5 min and were analyzed using a glucose analyzer. The temperature of the ear was constantly maintained with a closed-loop thermoelectric cooling temperature control of the plate containing the sapphire window. The dog's glucose concentration was clamped at eight different levels within the range 5.6 to 25.6 mM (100 to 460 mg/dL). Each clamping level lasted for approximately 35 min. During the course of the experiment, Raman spectra were continuously collected with 1.8 s per frame and a 1.6 s data transfer time, giving a frame every 3.4 s. (The duty cycle was limited by data transfer.) The laser was not shuttered during the file transfer. Each frame has pixel dimensions 260 (V) × 1340 (H) as hardware binning of every five vertical pixels was chosen. After data collection, the curvature correction algorithm was applied to all frames before vertical binning.[37] Since various frame-averaging schemes were adopted, the individual spectra are referred to as "frames" though they are one-dimensional, and the subsequent averaged spectra are referred to as "sample spectra."

Figure 3 shows the examples of the 33-frame averaged sample spectra with ~18.7 min between successive spectra. Apparent sapphire Raman peaks and a broadband decreasing
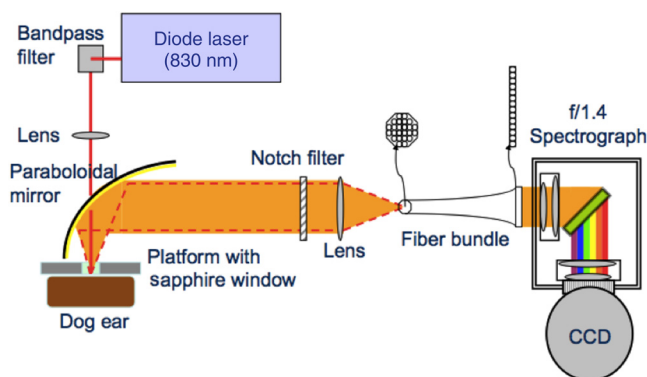

Fig. 2 The dog was positioned on its stomach with the ear positioned over the sapphire window aperture of the aluminum sample stage.

background are observed. To better accentuate Raman peaks from the dog ear, a fifth-order polynomial background subtraction routine was employed and the background removed spectrum is also shown in Fig. 3 with prominent sapphire peaks.

3 Results and Discussions

3.1 Minimum Detection Error Analysis

For a nearly shot-noise limited spectrum measurement, the minimum detection error can be estimated using experimental parameters such as signal-to-noise ratio (SNR) and an overlap factor.[15] To estimate spectral random noise, we calculated the variance of each pixel among 10 adjacent frames (frame 6485 to 6494). The rational for selecting these frames is to minimize the apparent variance owing to the background decay. The decay was observed to diminish with time. The calculated two-dimensional variance map was then processed by the curvature correction algorithm previously described and a single spectrum of variance was obtained. The estimated noise value, 360, was obtained from the average across the square root of the variance spectrum.
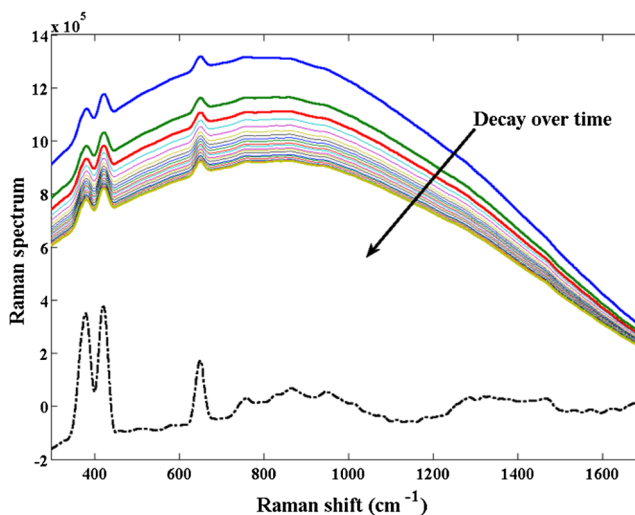

Fig. 1 Raman system configuration for the dog study.

Fig. 3 33-frame averaged sample spectra with ~18.7 min in between 2 adjacent spectra. A background removed spectrum is shown below.

The Raman spectrum of glucose was obtained from a 50-mM glucose water solution contained in the dog-ear-like sapphire sample holder. The norm of the glucose signal was calculated to be ~56 mM^{-1} using either a pixel range 240 to 1040 or 200 to 1200. The overlap factor for the experiment was estimated to be ~1.2 to 1.4 using the nine-component model described earlier. Using a previously developed theory, the minimum detection error based on these experimental parameters is ~8.36 to 9 mM (using raw frames).[15] If frame averaging is performed, ΔC is 1.46 to 1.57 mM and 1.04 to 1.11 mM for 33- and 65- frame averaging, respectively. Note that the ΔC formalism considers only random noise in the predicted spectra, not the calibration spectra nor the reference concentration, i.e., an absolutely correct model.

3.2 Preprocessing

Additional preprocessing steps were implemented besides the background removal mentioned earlier. Among the 6498 frames, we observed that the laser intensity fluctuated at two fixed frequencies, causing fluctuations at the same frequencies in the collected frames. Fourier filtering was employed to effectively remove the slowly varying laser intensity fluctuations. Owing to the high SNR, the charge-coupled device fixed pattern noise was very significant. We first heavily smoothed the sample spectrum using a 101-point Savitzky–Golay filter and then subtracted the smoothed spectrum from the original sample spectra to identify the fixed pattern noise. The fixed pattern noise in individual frames was subsequently removed according to intensity levels.

3.3 Partial Least Squares Analysis with Cross Validation

Various datasets were formed for PLS analysis using leave-one-out cross validation with differences in the following aspects:

number of frames averaged; with or without 25-pt Savitzky–Golay smoothing; and spectral range selection.

The results give us a general evaluation of the performance of our technique. Figures 4(a) to 4(d) show example results from one analysis with 33-frame averaging, 25-pt smoothing, and the plasma glucose as the reference concentration. Figure 4(a) shows the calculated root-mean-square error of the cross validation (RMSECV) versus number of PLS factors. The observed minimum indicates that the optimal calibration model contains eight factors. The Clark's error grid is plotted in Fig. 4(b) using the predicted concentrations obtained from the cross-validation procedure. This type of grid analysis is used by physicians to evaluate the performance of glucose analysis technologies. Predictions falling in zones A and B are clinically considered acceptable. Figure 4(c) compares the reference to the predicted glucose concentration over time (~1.87 min between two samples). The regression vector and glucose Raman spectrum are plotted in Fig. 4(d). Distinctive similarities are observed between the two, indicating that glucose was indeed measured because there was no prior glucose spectral information supplied to the PLS model. Table 1 lists all results from the cross-validation analyses with various calibration set formations.

3.4 Partial Least Squares Analysis with Cross Validation and Prediction

We then picked one set of parameters, i.e., 33-frame averaging and 25-pt smoothing, to perform further analysis with level splitting. Because the 65-frame averaging scheme did not give much improved RMSECV and results in fewer samples, analyses here were done using a 33-frame averaging. All the samples collected at the clamping levels were divided into a calibration set and a prediction set. Building calibration models solely based on the leveled data avoids additional confounding factors during the glucose rise and fall phases. PLS was performed on the
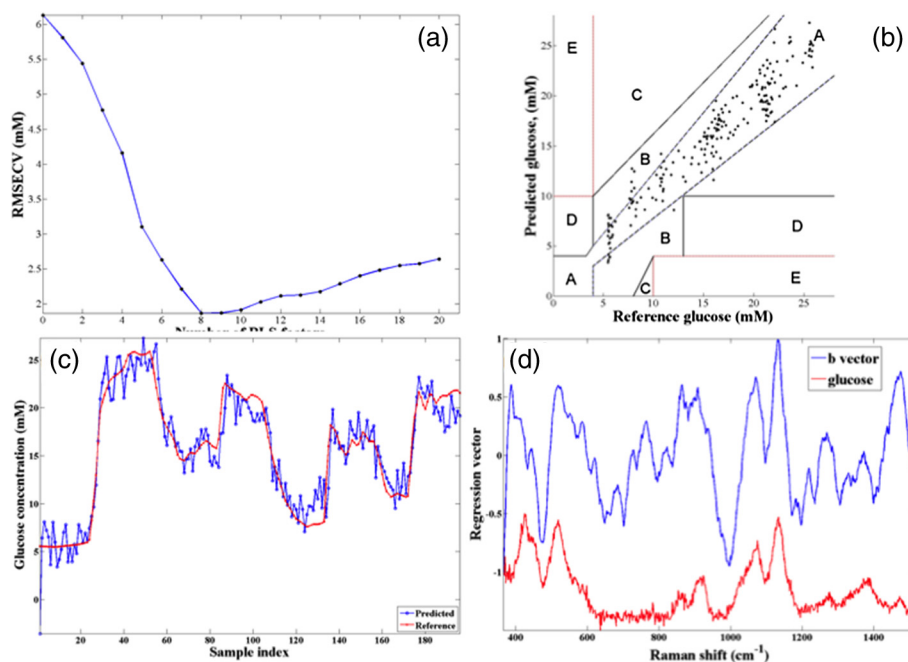

Fig. 4 Summary results from one analysis: (a) root-mean-square error of cross validation (RMSECV) versus number of partial least squares (PLS) factors; (b) Clark's error grid of RMSECV; (c) temporal profiles of reference and predicted glucose concentrations (~1.87 min between two samples); (d) regression vector (blue) and the glucose Raman spectrum (red).

Table 1 Cross-validation analysis with various preprocessing and parameters.

Preprocessing	Statistics	
	RMSECV (mM)	R^2
65f, 365 – 1519 cm^{-1}	2.03	0.89
65f, 25 pt, 365 – 1519 cm^{-1}	1.84	0.91
65f, 25 pt, 297–628 cm^{-1}	2.91	0.77
65f, 25 pt, 297–1703 cm^{-1}	1.56	0.93
65f, 25 pt, 1–1703 cm^{-1}	1.83	0.79
65f, 25 pt, 297 – 1703 cm^{-1}, 5op	1.72	0.92
33f, 365–1519 cm^{-1}	2.06	0.89
33f, 25 pt, 365–1519 cm^{-1}	1.87	0.91
33f, 25 pt, 297–628 cm^{-1}	3.10	0.74
33f, 25 pt, 297–1703 cm^{-1}	1.65	0.93
33f, 25 pt, 1–1703 cm^{-1}	1.67	0.93
33f, 25 pt, 297 – 1703 cm^{-1} 5op	1.76	0.92

calibration set to calculate RMSECV and the **b** vector, which was subsequently used to predict on the prediction set with the root-mean-square error of prediction (RMSEP). The **b** vector was then used to predict on all samples except the calibration samples, excluding the samples during glucose rise and fall phases, to calculate RMSEP$_1$, and including the samples during glucose rise or fall phases to calculate RMSEP$_2$ and R^2. Table 2 lists all results from the level-splitting analysis. The higher values observed in RMSEP$_2$ suggest that the divergence between ISF and plasma glucose is significant during the glucose rise and fall phases, which could not be corrected for using the calibration models based on leveled regions. These RMSEP values agree with the minimum detection error estimated earlier.

The next analysis was to form the calibration set with one level entirely left out, and then predict on the left-out level (RMSEP$_1$) and all samples not included in the calibration set (RMSEP$_2$). Results are summarized in Table 3. It is observed that the RMSEP$_2$ for level 1 is much higher than for other levels. This is because fluorescence photobleaching was most

Table 2 Level-splitting analysis with various preprocessing and parameters.

Reference wavenumber range	Statistics			
	RMSECV (mM)	RMSEP$_1$ (mM)	RMSEP$_2$ (mM)	R^2
365 – 1519 cm^{-1}	1.78 ± 0.18	1.77 ± 0.22	2.19 ± 0.24	0.93 ± 0.01
297–1703 cm^{-1}	1.78 ± 0.18	1.77 ± 0.22	2.19 ± 0.24	0.94 ± 0.01
297–1703 cm^{-1}, 5op	1.47 ± 0.14	1.4 ± 0.12	2.06 ± 0.09	0.94 ± 0.01

Table 3 Leave-one-level-out analysis with various preprocessing and parameters.

Preprocessing	Statistics			
	RMSECV (mM)	RMSEP$_1$ (mM)	RMSEP$_2$ (mM)	R^2
Level 1	1.81 ± 0.17	1.84 ± 0.29	4.83 ± 2.55	0.83 ± 0.08
Level 2	1.9 ± 0.25	1.88 ± 0.26	2.66 ± 0.55	0.92 ± 0.03
Level 3	1.84 ± 0.24	1.88 ± 0.26	2.81 ± 0.49	0.91 ± 0.03
Level 4	1.89 ± 0.19	1.85 ± 0.23	2.82 ± 0.54	0.91 ± 0.03
Level 5	1.83 ± 0.42	1.76 ± 0.27	2.73 ± 0.34	0.90 ± 0.03
Level 6	1.89 ± 0.34	1.83 ± 0.55	2.25 ± 0.58	0.93 ± 0.02
Level 7	1.88 ± 0.14	1.82 ± 0.26	2.38 ± 0.27	0.92 ± 0.02
Level 8	1.63 ± 0.14	1.63 ± 0.23	3.08 ± 0.29	0.87 ± 0.03

Table 4 Randomized concentration analysis.

Preprocessing	Statistics			
	RMSECV (mM)	RMSEP$_1$ (mM)	RMSEP$_2$ (mM)	R^2
Scheme 1	7.56 ± 0.78	7.56 ± 0.5	7.72 ± 0.4	0.06 ± 0.07
Scheme 2	7.83 ± 14	7.94 ± 0.61	7.72 ± 0.5	−0.01 ± 0.07

significant during that time and also the instrument and experimental subject needed a warm up time.

Finally, two randomized concentration profiles were used to demonstrate that the previous calibration models are indeed predictive. In the first case, random concentrations in the experimental range were paired with measured spectra. In the second case, the order of the reference concentration measurements was randomly scrambled. As shown in Table 4, result from these tests suggests RMSEP >7.5 mM with a model that lacks prediction capability. Therefore, results from previous calibration models are predictive for glucose concentration.

4 Conclusions

This paper describes an *in vivo* survival dog study performed on a beagle anesthetized for ∼8 h, during which its blood glucose concentration was clamped at several different levels. A glucose clamping study allows better disentangling of systematic effects from real glucose changes. Raman spectra were continuously acquired from the ear and reference blood glucose measurements were taken via venous blood draw. Using only the level data, RMSEP on the order of 1.5 to 2 mM (10% of the average concentration) was obtained, agreeing with the minimum detection error analysis. This RMSEP is higher than needed for diabetic patients. However, the average glucose level in the dog study (∼15 mM) was significantly higher than the fasting concentration in human subjects. Since it is critically important to accurately determine glucose concentration near hypoglycemia, future experimental designs will include

lower clamping concentrations. Distinctive similarities were observed between the resulting **b** vector and the glucose Raman spectrum measured in water, indicating that glucose was indeed measured. We have identified the photobleaching of tissue autofluorescence to be a key error source from the results of the leave-level 1-out analysis. A potential strategy for a mitigating scheme was suggested.[38] Results from this study demonstrate the feasibility of detecting glucose *in vivo* using transcutaneous Raman spectroscopy. In addition, the analyses and results provide valuable insights for improving our technique for future studies.

Acknowledgments

References

1. W. C. Shih, K. L. Bechtel, and M. S. Feld, *Handbook Of Optical Sensing Of Glucose In Biological Fluids And Tissues*, CRC Press, New York (2008).
2. V. Tuchin, *Tissue Optics: Light Scattering Methods and Instruments for Medical Diagnosis*, 2nd ed., SPIE Press Monograph, Bellingham, Washington (2007).
3. M. G. Ghosn, V. V. Tuchin, and K. V. Larin, "Depth-resolved monitoring of glucose diffusion in tissues by using optical coherence tomography," *Opt. Lett.* **31**(15), 2314–2316 (2006).
4. K. L. Bechtel, W. C. Shih, and M. S. Feld, "Intrinsic Raman spectroscopy for quantitative biological spectroscopy Part II: experimental applications," *Opt. Express* **16**(17), 12737–12745 (2008).
5. W. C. Shih, K. L. Bechtel, and M. S. Feld, "Intrinsic Raman spectroscopy for quantitative biological spectroscopy Part I: theory and simulations," *Opt. Express* **16**(17), 12726–12736 (2008).
6. J. Zeng et al., "Analysis of ethyl and methyl centralite vibrational spectra for mapping organic gunshot residues," *Analyst* **139**(17), 4270–4278 (2014).
7. G. J. Puppels et al., "Studying single living cells and chromosomes by confocal Raman microspectroscopy," *Nature* **347**(6290), 301–303 (1990).
8. A. Mahadevan-Jansen et al., "Near-infrared Raman spectroscopy for *in vitro* detection of cervical precancers," *Photochem. Photobiol.* **68**(1), 123–132 (1998).
9. A. J. Berger et al., "Multicomponent blood analysis by near-infrared Raman spectroscopy," *Appl. Opt.* **38**(13), 2916–2926 (1999).
10. K. Maquelin et al., "Raman spectroscopic method for identification of clinically relevant microorganisms growing on solid culture medium," *Anal. Chem.* **72**(1), 12–19 (2000).
11. H. Ding et al., "Development of Raman spectral markers to assess metastatic bone in breast cancer," *J. Biomed. Opt.* **19**(11), 111606 (2014).
12. N. Sudheendran et al., "Line-scan Raman microscopy complements optical coherence tomography for tumor boundary detection," *Laser Phys. Lett.* **11**(10), 105602 (2014).
13. Y. Li et al., "Micro-Raman spectroscopy study of cancerous and normal nasopharyngeal tissues," *J. Biomed. Opt.* **18**(2), 027003 (2013).
14. A. M. K. Enejder et al., "Raman spectroscopy for noninvasive glucose measurements," *J. Biomed. Opt.* **10**(3), 031114 (2005).
15. O. R. Scepanovic et al., "Determination of uncertainty in parameters extracted from single spectroscopic measurements," *J. Biomed. Opt.* **12**(6), 064012 (2007).
16. W. C. Shih, K. L. Bechtel, and M. S. Feld, "Constrained regularization: hybrid method for multivariate calibration," *Anal. Chem.* **79**(1), 234–239 (2007).
17. W.-C. Shih, K. Bechtel, and M. Feld, *In Vivo Glucose Measurements*, John Wiley & Sons, Inc. (2009).
18. J. Qi and W.-C. Shih, "Parallel Raman microspectroscopy using programmable multi-point illumination," *Opt. Lett.* **37**(8), 1289–1291 (2012).
19. J. Qi, J. Li, and W.-C. Shih, "High-speed hyperspectral Raman imaging for label-free compositional microanalysis," *Biomed. Opt. Express* **4**(11), 2376–2382 (2013).
20. J. Qi and W. C. Shih, "Performance of line-scan Raman microscopy (LSRM) for high-throughput chemical imaging of cell population," *Appl. Opt.* **53**(13), 2881–2885 (2014).
21. Z. W. Huang et al., "Rapid near-infrared Raman spectroscopy system for real-time *in vivo* skin measurements," *Opt. Lett.* **26**(22), 1782–1784 (2001).
22. M. S. Bergholt, W. Zheng, and Z. Huang, "Development of a multiplexing fingerprint and high wavenumber Raman spectroscopy technique for real-time *in vivo* tissue Raman measurements at endoscopy," *J. Biomed. Opt.* **18**(3), 030502 (2013).
23. M. M. P. Arnob et al., "Laser rapid thermal annealing enables tunable plasmonics in nanoporous gold nanoparticles," *Nanoscale* **6**(21), 12470–12475 (2014).
24. F. Zhao et al., "Monolithic NPG nanoparticles with large surface area, tunable plasmonics, and high-density internal hot-spots," *Nanoscale* **6**(8199–8207 (2014).
25. J. Zneg et al., "Internal and external morphology-dependent plasmonic resonance in monolithic nanoporous gold nanoparticles," *RSC Adv.* **4**(36682–36688 (2014).
26. J. Qi et al., "Surface-enhanced Raman spectroscopy with monolithic nanoporous gold disk substrates," *Nanoscale* **5**(10), 4105–4109 (2013).
27. H. Wang et al., "Quantitative analysis of creatinine in urine by metalized nanostructured parylene," *J. Biomed. Opt.* **15**(2), 027004 (2010).
28. M. Li et al., "Microfluidic surface-enhanced Raman scattering sensor with monolithically integrated nanoporous gold disk arrays for rapid and label-free biomolecular detection," *J. Biomed. Opt.* **19**(11), 111611 (2014).
29. K. W. Kho et al., "Polymer-based microfluidics with surface-enhanced Raman-spectroscopy-active periodic metal nanostructures for biofluid analysis," *J. Biomed. Opt.* **13**(5), 054026 (2008).
30. J. Qi et al., "Label-free, in situ SERS monitoring of individual DNA hybridization in microfluidics," *Nanoscale* **6**(15), 8521–8526 (2014).
31. P. Z. McVeigh et al., "Widefield quantitative multiplex surface enhanced Raman scattering imaging *in vivo*," *J. Biomed. Opt.* **18**(4), 046011 (2013).
32. M. Li et al., "Stamping surface-enhanced Raman spectroscopy for label-free, multiplexed, molecular sensing and imaging," *J. Biomed. Opt.* **19**(5), 050501 (2014).
33. S. M. Stranahan and K. A. Willets, "Super-resolution optical imaging of single-molecule SERS hot spots," *Nano Lett.* **10**(9), 3777–3784 (2010).
34. J. L. Lambert et al., "Measurement of aqueous glucose in a model anterior chamber using Raman spectroscopy," *J. Raman Spectrosc.* **33**(7), 524–529 (2002).
35. P. J. Caspers, G. W. Lucassen, and G. J. Puppels, "Combined *in vivo* confocal Raman spectroscopy and confocal microscopy of human skin," *Biophys. J.* **85**(1), 572–580 (2003).
36. C. A. Lieber et al., "Raman microspectroscopy for skin cancer detection *in vitro*," *J. Biomed. Opt.* **13**(2), 024013 (2008).
37. J. Qi, K. L. Bechtel, and W.-C. Shih, "Automated image curvature assessment and correction for high-throughput Raman spectroscopy and microscopy," *Biomed. Spectrosc. Imaging* **3**(4), 359–368 (2014).
38. H. Wang et al., "Improving skin Raman spectral quality by fluorescence photobleaching," *Photodiagn. Photodyn. Ther.* **9**(4), 299–302 (2012).

Biographies of the authors are not available.